In Vivo Imaging of Schlemm's Canal and Limbal Vascular Network in Mouse Using Visible-Light OCT

Xian Zhang,[1,2] Lisa Beckmann,[2] David A. Miller,[2] Guangbin Shao,[3] Zhen Cai,[1,2] Cheng Sun,[3] Nader Sheibani,[4] Xiaorong Liu,[5] Joel Schuman,[6] Mark Johnson,[2,8] Tsutomu Kume,[7] and Hao F. Zhang[2,8]

[1]Department of Ophthalmology, Tongji Medical College, HuaZhong University of Science and Technology, Wuhan, Hubei, China
[2]Department of Biomedical Engineering, Northwestern University, Evanston, Illinois, United States
[3]Department of Mechanical Engineering, Northwestern University, Evanston, Illinois, United States
[4]Department of Ophthalmology and Visual Science, University of Wisconsin, Madison, Wisconsin, United States
[5]Department of Biology and Psychology, University of Virginia, Charlottesville, Virginia, United States
[6]Department of Ophthalmology, New York University, New York, New York, United States
[7]Department of Medicine, Northwestern University, Chicago, Illinois, United States
[8]Department of Ophthalmology, Northwestern University, Chicago, Illinois, United States

Correspondence: Hao F. Zhang, Department of Biomedical Engineering, 2145 Sheridan Road, Evanston, IL 60208, USA; hfzhang@northwestern.edu.

XZ and LB contributed equally to this work.

Received: August 14, 2019
Accepted: December 5, 2019
Published: February 18, 2020

Citation: Zhang X, Beckmann L, Miller DA, et al. In vivo imaging of Schlemm's canal and limbal vascular network in mouse using visible-light OCT. *Invest Ophthalmol Vis Sci.* 2020;61(2):23. https://doi.org/10.1167/iovs.61.2.23

Purpose. To validate the ability of visible-light optical coherence tomography (vis-OCT) in imaging the full Schlemm's canal (SC) and its surrounding limbal vascular network in mice in vivo through a compound circumlimbal scan.

Methods. We developed an anterior segment vis-OCT system and a compound circumlimbal scanning method, which montages eight rotated raster scans. We calibrated the circumlimbal scan geometry using a three-dimensional printed phantom eyeball before imaging wild-type C57BL/6J mice. We measured SC size by segmenting SC cross sections from vis-OCT B-scan images and imaged the limbal microvascular network using vis-OCT angiography (vis-OCTA). To introduce changes in SC size, we used a manometer to adjust the intraocular pressure (IOP) to different levels. To create additional optical scattering contrast to enhance SC imaging, we surgically increased the episcleral venous pressure (EVP) and caused blood reflux into SC.

Results. Using the compound circumlimbal scan, our anterior segment vis-OCT noninvasively imaged the full SC and limbal microvascular network in mouse for the first time. We observed an average 123% increase in SC volume when we decreased the IOP by 10 mm Hg from the baseline IOP of 7 to 10 mm Hg and an average 72% decrease in SC volume when the IOP level was elevated by 10 mm Hg from the baseline IOP. We also observed location-dependent SC size responses to IOP changes. Blood reflux caused by increased EVP enabled vis-OCTA to directly visualize SC, which matched well with the segmented SC.

Conclusions. Vis-OCT and vis-OCTA can accurately image the entire SC and limbal microvascular network in vivo using the compound circumlimbal scan. Vis-OCT is also able to quantitatively measure SC responses to changing IOP levels.

Keywords: optical coherence tomography, angiography, Schlemm's canal

Glaucoma is the second most common cause of irreversible blindness, impairing 80 million people worldwide.[1] Elevated intraocular pressure (IOP) is the most common indicator for diagnosis and progression of glaucoma, with reduction of IOP the only proven glaucoma intervention.[2–4] IOP is controlled by the balance between production and outflow of aqueous humor. In the conventional outflow pathway, the aqueous humor travels through the trabecular meshwork and juxtacanalicular connective tissue (JCT), into Schlemm's canal (SC), through collector channels (CCs) passing through the sclera, and finally emptying into the episcleral veins.[5,6] The increased IOP characteristic of primary open-angle glaucoma is caused by increased resistance to aqueous humor outflow.[7,8] Most investigations of outflow resistance have focused on the JCT and inner wall of SC, which are widely regarded as the principal sites of outflow resistance.[9] However, flow resistance is also generated in SC and CCs, particularly in the former as IOP is increased.[8,9]

In primate, humans, and mice, SC is essentially a flat tube traveling circumferentially around the limbus of the eye, whose opening thickness, the distance from the inner wall to outer wall, decreases as IOP increases.[9] Greater lengths of SC are collapsed in glaucomatous eyes than healthy eyes,

even when perfused at the same IOP,[10] and such collapse has been speculated to contribute to the elevated IOP characteristic of glaucoma.[11–13]

A clinical practice to improve visualization of SC is to increase pressure of the downstream episcleral veins so that blood flows backward from the normal path and into SC. Recent studies have shown that the quality of such blood reflux into SC immediately before or during surgery (both selective laser trabeculoplasty and canaloplasty) correlates with the success of the surgery and postsurgery IOP levels.[14,15] As a result, a method that can noninvasively image the outflow pathway will bring significant benefits to both clinical and preclinical investigations. We seek to image SC and associated limbal microvascular network in the mouse using optical coherence tomography (OCT).

OCT is widely used in noninvasive ophthalmic imaging,[16] which provides in vivo anatomical and functional information of both the anterior and posterior eyes at an axial resolution of several micrometers.[17,18] Researchers have used OCT to investigate properties of SC in vivo in mice and humans.[17,19–26] These studies were limited in axial resolution (2–5 μm) and field of view (0.5–3 mm). Imaging the detailed structure of SC in mice requires overcoming several hurdles. First, the relatively small size of SC, especially in mice, requires a higher resolution to reveal the details of SC and to investigate the variation of SC in different conditions. Second, SC is a circular channel located around the limbus, with optimal image quality occurring when the OCT probing light is perpendicular to the curvature of the eye at the location of SC. However, existing OCT systems are usually designed such that the incident light is along the optical axis of the eye, requiring the mouse to be tilted significantly to optimally image SC. Third, the extreme variations in SC size and shape within a single mouse eye suggest that it is important to image the entire SC instead of a certain section of SC. If the entire SC is imaged with a traditional OCT system, the mouse must be rotated. When rotating the mouse, the IOP and SC size become unstable, where mouse demonstrates higher IOP and smaller SC when the head is lower than the body.[27] Additionally, it has previously been shown that episcleral venous pressure (EVP) can also vary with the angle of the mouse body, affecting the natural outflow of aqueous humor.[27]

To overcome these challenges, we developed an anterior segment visible-light OCT (vis-OCT) to conduct a circumlimbal scan and image the whole SC without rotating the mouse. Vis-OCT is a newly developed OCT technology, which uses visible light as its light source rather than the commonly used near-infrared light in commercial OCT systems.[28–30] Using shorter wavelengths allows for higher axial resolution for a given bandwidth and higher backscattering sensitivity in tissue.[31,32] The higher axial resolution allows more precise measurement of SC anatomy as well as SC changes. Additionally, taking advantage of improved sensitivity to slow blood flow, vis-OCT angiography (vis-OCTA) has the potential to better visualize the superficial limbal microvasculature and the outflow veins downstream from SC.

In this study, we first validated our vis-OCT's capability to measure the morphology of SC at an axial resolution of approximately 1 µm in a three-dimensional (3D) printed phantom eyeball and in wild-type mice. Then, we artificially adjusted the IOPs in wild-type mice using a manometer and investigated SC cross-sectional size change with IOP. In addition, we introduced blood reflux into SC and showed that the backscattering contrast provided by blood reflux into SC allows for direct visualization of SC using vis-OCTA. Finally, we visualized the entire SC and its surrounding limbal microvascular network in 3D using a compound circumlimbal scan.

Methods and Materials

Animal Preparation

Our experimental protocol was approved by the Northwestern University Institutional Animal Care and Use Committee and conformed to the Association for Research in Vision and Ophthalmology Statement on Animal Research. We used adult wild-type C57BL/6 mice approximately 3 months old in our experiments. The mice were kept under normal lighting conditions with 12-hour-on, 12-hour-off cycles in the Center for Comparative Medicine at Northwestern University. Prior to any imaging or procedure, the mice were anesthetized by intraperitoneal injection (10 mL/kg body weight) of a ketamine/xylazine cocktail (ketamine: 11.45 mg/mL; xylazine: 1.7 mg/mL, in saline). During imaging, the mouse's body temperature was maintained by a heating lamp, and a pulse oximeter was attached to the left rear paw to monitor peripheral arterial sO_2 and heart rate. After imaging, the animals were placed in a warm cage for recovery, and toe/tail pinch withdrawal, heart rate, breath rate, and sO_2 were monitored every 20 minutes until fully recovered.

Experimental System Setup

Figure 1a shows the schematic of the experimental vis-OCT system. Briefly, light from a supercontinuum laser (SuperK EXTREME; NKT Photonics, Birkerød, Denmark) was filtered and sent to a 30:70 fiber coupler (Gould Fiber Optics, Millersville, MD). A pair of galvanometer mirrors (Nutfield Technology, Londonderry, NH) scanned the beam through an objective lens (LSM03, ThorLabs, Newton, NJ; SL in Fig. 1a), which focused the light onto the sample. Prior to the objective lens, the beam diameter was 2 mm. A visible light spectrometer (Blizzard SR; Opticent Health, Evanston, IL) operating from 510 to 610 nm detected the interferogram signals for image reconstruction. The theoretical axial and lateral resolutions of the system were 1.3 and 6.8 µm, respectively.

Due to the anatomical location of SC in the anterior segment, either the mouse eye or the vis-OCT light beam needs to tilt approximately 60° from the optical axis of the eye to best image SC and the limbus. Because tilting the mouse by such a large angle has been shown to affect EVP,[27] we chose to tilt the light beam 60° using a two-mirror assembly (Fig. 1b) to avoid unwanted EVP elevation-induced SC perturbation. We mounted this assembly and the objective lens on a motorized rotational stage (PRM1Z8; ThorLabs). We rotated the two-mirror assemble and objective lens eight times at a step size of 45° about the ocular axis (Fig. 1a, dashed line) and performed a raster scan at each rotational step. As a result, we created a compound circumlimbal scan to image the full SC and limbal microvascular network while the mouse stayed stationary.

IOP-Level Control

We cannulated the anterior chamber and manometrically set the IOP level in the mouse (Fig. 1c). We first used a 33-gauge lancet to create a hole near the limbus, then placed

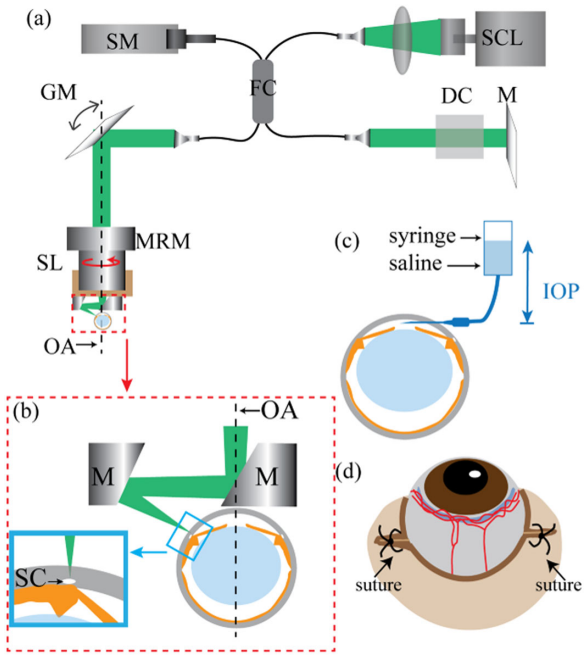

Figure 1. (**a**) Schematic of the vis-OCT system. DC, dispersion compensation; FC, fiber coupler; GM, galvanometer mirrors; M, mirror; MRM, motorized rotational mount; SCL, supercontinuum light source; SL, scan lens; SM, spectrometer; OA, optical axis of the eye, which is also the axis of rotation of the motorized rotational mount. (**b**) Detailed illustration of the components being highlighted by the *red dashed box* in panel (**a**). M, mirror; OA, optical axis; SC, Schlemm's canal. The incident light reflects off both the mirrors after the SL, such that it is angled perpendicularly to the surface of the eye at SC, as shown in the *blue* inset. (**c**) Illustration of the cannulation of the anterior chamber with an open syringe filled with physiologic saline, whose height can be adjusted to set IOP levels in the mouse eye. (**d**) Illustration of sutures to cause blood reflux into SC.

a blunt 34-gauge needle through that hole. This 34-gauge needle was stabilized by attaching it to an external support. As shown in Figure 1c, we connected the needle to an open syringe filled with physiologic saline. The height of the syringe manometrically controlled the IOP. We used a tonometer (TonoLab Tonometer, Icare, Finland) to measure the IOP values of the mouse eyes. We confirmed the height to set the saline column for baseline (Δ0) IOP position by using the tonometer. In our study, we adjusted the IOP to be ±10 mm Hg and ±5 mm Hg with respect to the baseline IOP, which varied from 7 to 10 mm Hg and agreed with a previously published average baseline IOP in wild-type C57BL/6 mice anesthetized with ketamine and xylazine.[33] Using our real-time vis-OCT preview, we found that the shape and size of SC stabilized approximately 1 minute after changing the IOP. We allowed the eye to adjust to the each new IOP level for 3 minutes before acquiring a vis-OCT or vis-OCTA image. We also note that because of the needle in the anterior chamber, we will be unable to image the entire SC in manometry studies.

Episcleral Vein Blockage to Cause Blood Reflux

We cut approximately 1 to 2 mm at the outer canthus and added a suture (7-0 thread, using a round-tip needle) approximately 1 mm nasal of the original outer canthus (Fig. 1d). We then used forceps to gently squeeze the skin around the eyelid, causing the eye to slightly pop out of the eyelid. We then tightened the suture so that the eye could not fall back into the socket but remained slightly exposed.

Phantom Eyeball and Compound Circumlimbal Scan Calibration

To calibrate geometries of the eight raster scans to form a montage circumlimbal scan, we made a 3D-printed phantom eyeball, which had comparable size and geometry to a mouse eyeball (sphere, diameter: 3 mm). The phantom eyeball was also 3D printed to include an annular groove around the sphere at the approximate position of SC in the anterior segment. We heated a polyethylene (PE-50) tube and pulled it over a flame to reduce the inner diameter from approximately 530 µm to approximately 150 µm. Then we laid the tube into the groove to mimic SC and connected it via a blunt 23-gauge needle to a syringe placed in a micro pump (Harvard Apparatus, Holliston, MA). The mechanical drawing of the phantom eyeball is shown in Figure 2a, where the tube is colored yellow and flow direction is highlighted by the blue dashed arrows. We coated the phantom eyeball with ultraviolet-cured optical adhesive (Norland Optical Adhesive 81; Norland Products, Inc.), which contained ceramic scattering particles (200 nm) to mimic the highly scattering sclera.

Figure 2b shows a cross-sectional vis-OCT B-scan of the phantom eyeball, with highlighted hollow tube and coating layer. We diluted Intralipid (Millipore Sigma, Burlington, MA) to 2% with phosphate-buffered saline and flowed it through the tube (Fig. 2c) to create a positive contrast to image SC using vis-OCTA (Fig. 2d). We acquired eight raster scans, each after rotating the motorized mount 45°. In each raster scan, the two-mirror assembly tilted the beam 60° from the optical axis. To match this, each OCTA en face image was projected from a plane angled 60° from the optical axis and radially spaced 45° apart (Fig. 2e). Each projected image was manually fine adjusted to produce the final montaged image (Fig. 2f).

Finally, we quantified the accuracy of the montaged image. The defining characteristic of the phantom eyeball is the angle of the inlet and outlet grooves, which were designed to be precisely 45°. Using ImageJ (National Institutes of Health, Bethesda, MD, USA), we measured the angle of both the inlet and outlet tubing five times each in the final montaged image. The inlet tubing has a measured mean path angle of 45.1° ± 0.5° and the outlet tubing has a measured mean path angle of 44.4° ± 12°. To validate the accuracy of vis-OCT measurement of tube cross-sectional areas, we imaged a glass capillary tube (#1-000-800; Drummond Scientific Co., Broomall, PA) filled with water. Our measured inner diameter was 392 µm, which agreed well with the manufacturer's specified diameter of 400 µm.

Vis-OCT Imaging

Prior to vis-OCT imaging, we immobilized the mouse on a homemade holder. We first aligned the vis-OCT system without the two-mirror assembly so that the optical axis of the mouse eye aligned with the vis-OCT probing beam and the pupil was centralized. After we centered the eye, we mounted the two-mirror assembly for SC imaging, and if needed, we readjusted the vertical position of the mouse for better optical focusing. The oblique-incident vis-OCT beam

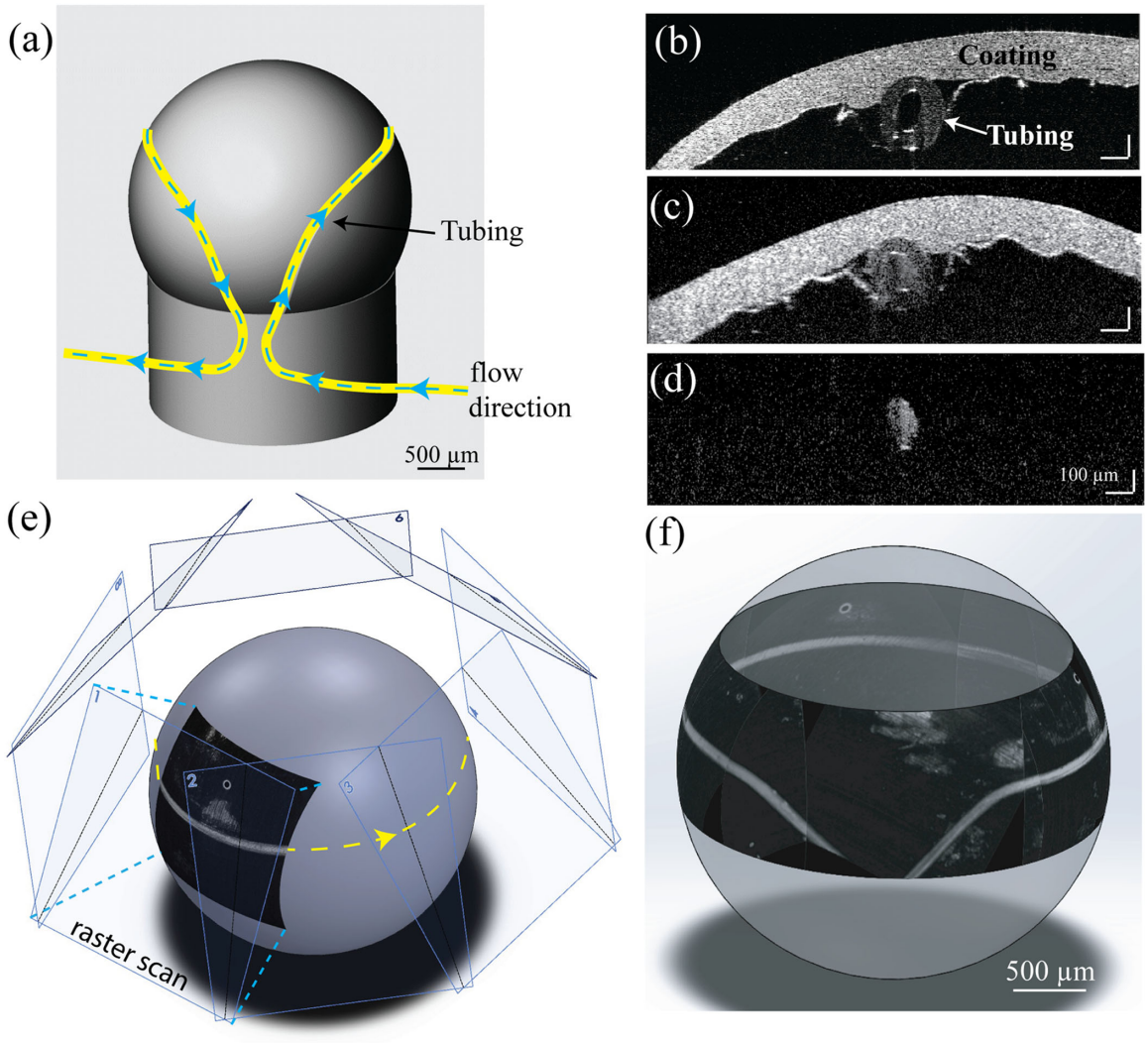

Figure 2. (**a**) Schematic of the 3D-printed phantom eyeball, with tube inset into groove shown in *yellow*. Direction of the Intralipid flow is shown with the *blue dashed line*. (**b**) Vis-OCT B-scan image of the phantom eyeball without flowing Intralipid. (**c**) Vis-OCT B-scan image of the phantom eyeball with flow Intralipid. (**d**) Vis-OCTA B-scan image of the phantom eyeball with flowing Intralipid. (**e**) Geometry of how the eight raster scans are montaged onto a sphere. (**f**) 3D visualization of the montaged image of the phantom eyeball.

was approximately perpendicular to the scleral plane. In the compound circumlimbal scan, each raster scan area was 1.8×1.8 mm^2, which covered roughly 20% of the perimeter of SC. For anatomical imaging, each raster scan contained 512 B-scans, and each B-scan contained 512 A-lines. For vis-OCTA imaging, we repeated each B-scan five times. The spectrometer integration time was 40 µs, and the vis-OCT illumination power was approximately 1.0 mW.

Image Processing and Montage

We developed a semiautomatic method to segment SC in vis-OCT B-scan using a custom MATLAB (Mathworks, Natick, MA, USA) program. Briefly, we upsampled the vis-OCT B-scan image 1580×2000 pixels and applied a mean filter (10×10 pixels). We then binarized the B-scan image based on a user-specified intensity threshold and automatically removed small structures that were less than 25 pixels in area. The user then clicks inside SC, and an automatic filling algorithm, based on morphologic reconstruction, extends from the pixel the user clicked outward until boundaries are reached on all sides. A change in intensity between a pixel and any of its four vertically or horizontally adjacent pixels creates a boundary.[34] If necessary, the user can manually modify the segmented boundary. For 3D visualization and volume measurement, we segmented SC from every other vis-OCT B-scan image. The spacing between segmented B-scan images is 7.4 µm, matching well with the theoretical lateral resolution (6.8 µm, Rayleigh criteria under Gaussian beam profile) of the vis-OCT system. As a result, the segmented B-scans are very close to both nonoverlapping and without gaps. After SC was segmented from all B-scans, we used open-source software (3D Slicer) to visualize it in 3D. To calculate cross-sectional area of SC, we multiplied the vis-OCT pixel size within a B-scan image with the total number of pixels within the segmented SC. To calculate SC volume, we summed all the cross-sectional areas within a selected SC segment and multiplied the total area with the corresponding B-scan thickness.

We validated the repeatability of our segmentation using a test-retest method, where we repeated the IOP-level control sequence twice back to back: first decreasing from

Investigative Ophthalmology & Visual Science

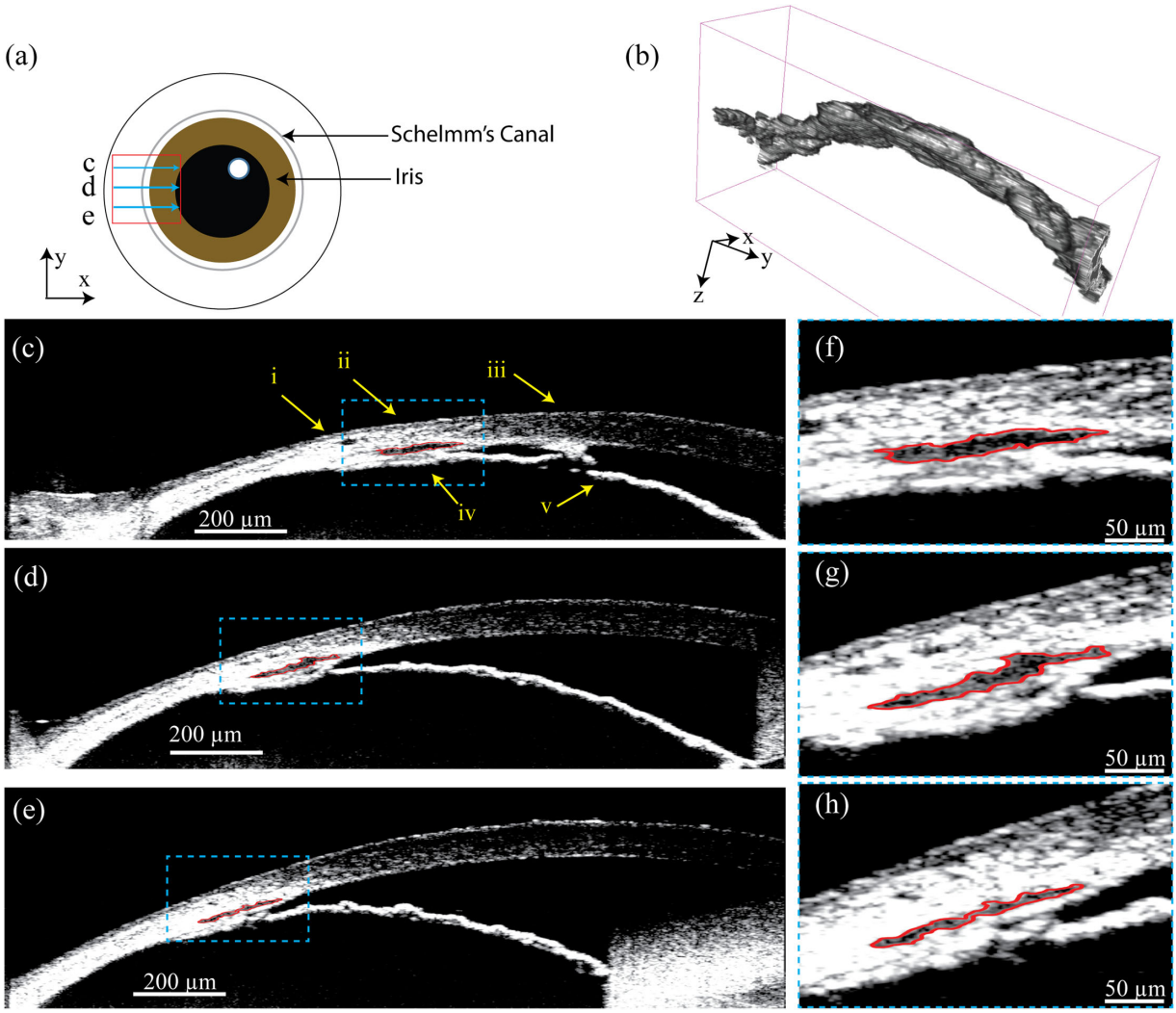

Figure 3. (**a**) Illustration of a top view of the mouse eye with positions and directions of three B-scans (*blue arrow*) shown within a raster scan (*red box*). (**b**) 3D visualization of the segmented SC from 270 adjacent B-scans, equivalent to 1 mm in length, with *x:y:z* aspect ratios of 1:2:3 (see Supplementary Video S1). Panels (**c**), (**d**), and (**e**) are vis-OCT B-scan images from the three positions highlighted in panel (**a**); SC is outlined in *red*. (i) sclera, (ii) limbus, (iii) cornea, (iv) ciliary body, and (v) iris. Panels (**f**), (**g**), and (**h**) are magnified views of SC corresponding to the areas highlighted in panels (**c**), (**d**), and (**e**), respectively.

Δ+10 mm Hg to Δ−10 mm Hg in steps of 5 mm Hg, then increasing from Δ−10 mm Hg to Δ+10 mm Hg in steps of 5 mm Hg. Before comparing the two data sets, we corrected lateral displacement through cross-correlation across 400 B-scans. We calculated the Pearson correlation coefficient between the two Δ−10-mm Hg data sets and between the two Δ+5-mm Hg data sets. The two Δ−10-mm Hg data sets were acquired successively without changing IOP values between two acquisitions. Their Pearson correlation coefficient was 0.81, representing a good match.[35] The two Δ+5-mm Hg data sets were acquired with a 24-minute delay and the six distinct IOP-level changes. The Pearson correlation coefficient between the two Δ+5 data sets was 0.66, representing a moderate match.[35] Please refer to Supplementary Figure S1 for more details.

For processing vis-OCTA data, we followed the method described by Chen et al.[36] To create a full-view SC image, we montaged and mapped the individual raster scans vis-OCTA en face images taken at different positions onto a sphere using Solidworks (Dassault Systems, Vélizy-Villacoublay, France) as illustrated in Figure 2e. Specifically, en face vis-OCTA images were projected onto the surface of a 3-mm-diameter sphere. To match the scanning geometry, each en face image was projected from a plane angled 60° from the vertical axis with each subsequent plane radially spaced 45° from the other. If needed, we manually readjust each projected image for better alignment as shown in Figure 2f. We compared the measured SC from both segmentation and vis-OCTA by calculating the Dice coefficient[37] in the respectively projected images.

Results

Figure 3 shows that the ultrahigh resolution vis-OCT imaging of the anterior segment reveals the large variation in the shape and size of SC, even within a 1-mm section. In Figure 3a, the red box highlights the approximate location of the imaged SC section and the three blue arrows highlight the scanning direction and locations of the B-scan

Investigative Ophthalmology & Visual Science

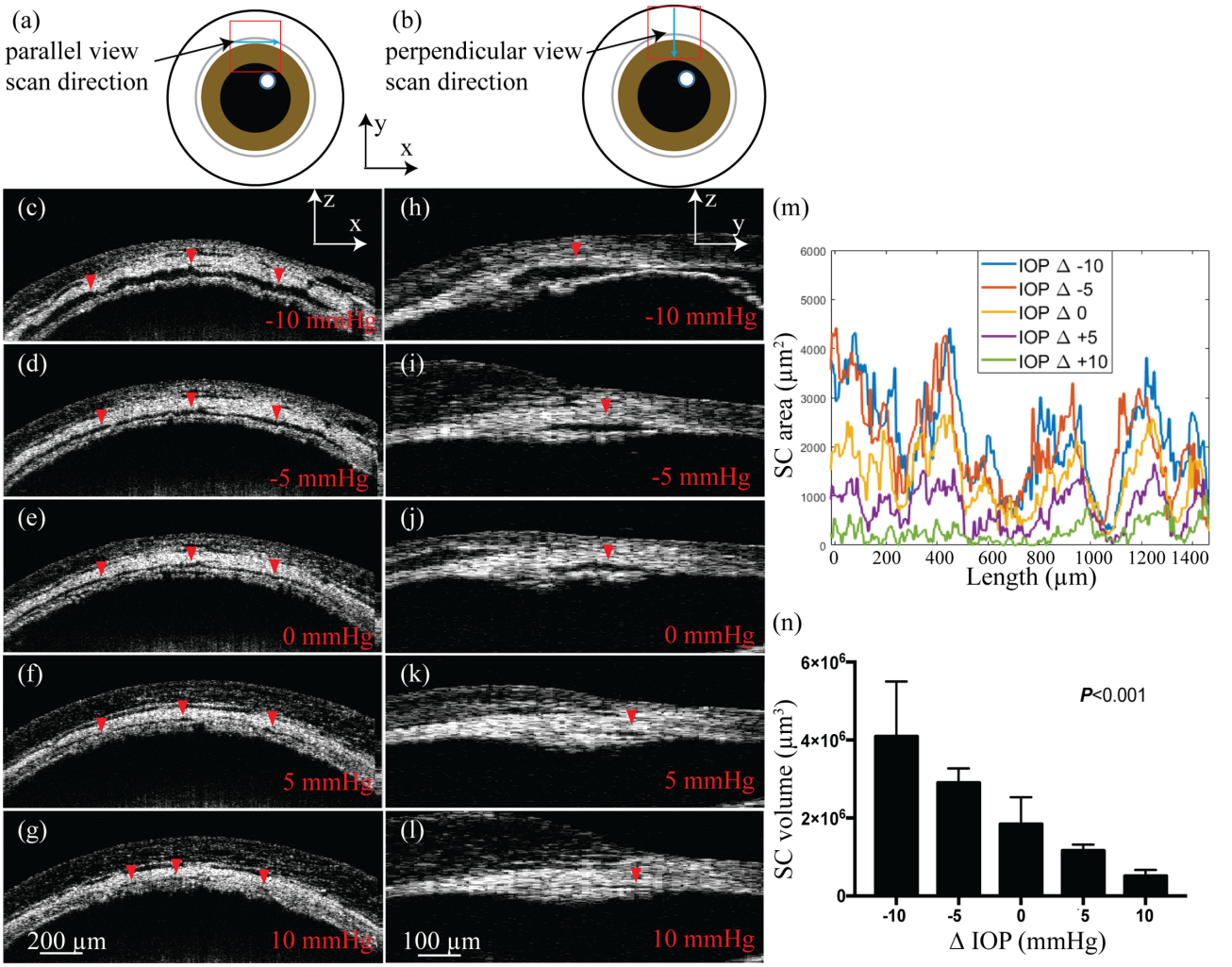

Figure 4. (**a**, **b**) Illustrations of a top view of the mouse eye with positions and directions of the parallel-view and perpendicular-view B-scan images, respectively. (**c–g**) Parallel-view vis-OCT images under different IOP levels from the position highlighted in panel (**a**). (**h–l**) Parallel-view vis-OCT images under different IOP levels from the position highlighted in panel (**b**). The *red arrowheads* highlight SC in the B-scan images. (**m**) Examples of SC cross-sectional area changes at different positions along the canal under different IOP levels. (**n**) Mean ± standard deviation volumes of 1.5-mm SC segments at IOP levels of –10 mm Hg, –5 mm Hg, 0 mm Hg, +5 mm Hg, and +10 mm Hg with respect to the baseline IOP.

images. Figure 3b shows the final result after surface rendering of a segmented 1-mm SC section using 3D Slicer, an open-source software.[38] The *x:y:z* aspect ratio was stretched to 1:2:3 for visualization purposes. Additionally, the model was smoothed along the *y*-axis (B-scan direction) across five B-scans. The two ends were not smoothed. Figures 3c–3e show three representative vis-OCT B-scan images (from the positions highlighted in Fig. 3a) used for segmentation and 3D visualization. We refer to these B-scan images as perpendicular views of SC. The segmented SC is outlined in red in each B-scan image. Due to lack of optical scattering contrast, the area inside SC shows noticeably lower vis-OCT intensity than the surrounding regions. We highlight the (i) sclera, (ii) limbus, (iii) cornea, (iv) ciliary body, and (v) iris in Figure 3c, which are landmarks to facilitate locating SC. The magnified views of the areas highlighted by the blue dashed boxes in Figures 3c–3e are respectively shown in Figures 3f–3h, where segmented SC sizes are 8743 µm^2, 8168 µm^2, and 4047 µm^2, respectively. The pixel size is approximately 1.1 µm along both the axial and lateral directions.

Figure 4 shows the results of imaging SC size variation under different monometrically set IOP levels. We visualized SC size variations along the canal (parallel view) and perpendicular to the canal (perpendicular view) from the approximate positions illustrated in Figures 4a and 4b, respectively. Figures 4c–4g show the parallel-view B-scan images of SC from the same position when we changed the IOP from –10 mm Hg to +10 mm Hg with respect to the baseline IOP at a step size of 5 mm Hg. In these parallel-view images, we can see the elongated cross section of the imaged SC (dark area highlighted by red arrowheads). Figures 4h–4l show perpendicular-view B-scan images taken from the position highlighted in Figure 4b under the same five different IOP levels. In both the parallel and perpendicular views, SC cross-sectional areas were obviously larger at a lower IOP and decreased in size as IOP increased. When the IOP was 10 mm Hg above the baseline IOP, SC nearly collapsed completely (Figs. 4g and 4l). At higher IOP levels (Figs. 4f–g, 4k–l), entire sections of SC appeared collapsed, for up to tens of microns in length.

Investigative Ophthalmology & Visual Science

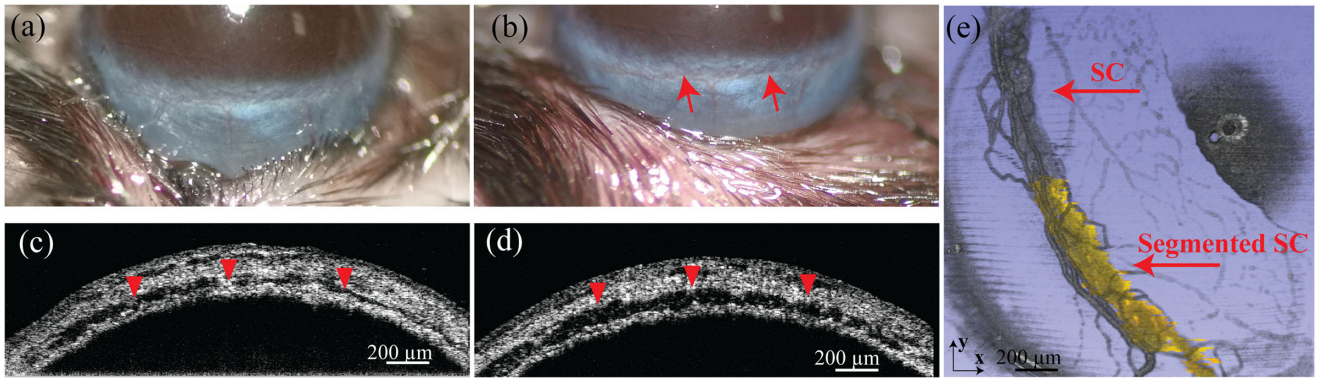

Figure 5. (**a**, **b**) Photos of mouse eyes without and with the episcleral vein blocked. The *red arrows* in (**b**) highlight SC after it is filled with blood. (**c**, **d**) Vis-OCT parallel-view B-scan images before and after blood reflux. The *red arrows* in both the photos and vis-OCT parallel-view B-scan images point to SC. (**e**) 3D visualization of SC with blood reflux imaged by vis-OCTA directly (*gray*) and overlaid segmentation result (*yellow*).

At each of the five IOP levels, we segmented an approximately 1.5-mm length of SC acquired in the perpendicular view, with a spacing of 7.4 μm between segmented B-scans. We calculated the cross-sectional area of SC (in μm^2) for each B-scan analyzed. The results of this analysis in one representative mouse are shown in Figure 4m, with SC areas plotted against B-scan positions. There appears to be a periodic pattern to the area increasing and decreasing, which remains true across all the IOP levels. This observation is consistent among all the mice imaged ($n = 8$). In addition, the change in SC volume against IOP level is further illustrated in Figure 4n.

Figure 5 shows the comparison between directly visualized SC based on blood reflux and results from segmenting the canal. We introduced blood reflux into SC through episcleral vein blockage to create optical scattering contrast inside SC as described in the Methods and Materials section and illustrated in Figure 1d. Taking advantage of the motion of refluxed red blood cells in SC, vis-OCTA can directly visualize SC. Figure 5a shows a normal mouse eye, with SC nearly invisible. After episcleral vein blockage, SC became bright red and clearly visible, confirming that blood was pushed back into SC (Fig. 5b). Figures 5c and 5d show the parallel-view vis-OCT B-scan images of SC from the same location before and after suturing. SC (dark region highlighted by the red arrowheads) is enlarged after EVP increase, indicating that SC is no longer in its natural physiologic state after blood reflux. With blood reflux, the size and shape of SC are similar to what we observed when IOP was 10 mm Hg below the baseline IOP level. A 3D visualization of vis-OCTA images covering a 1.8 mm × 1.8 mm area is shown in Figure 5e. SC is clearly visualized by vis-OCTA, which relies on motion contrast, confirming that blood reflux enhanced the imaging contrast of SC as a result of blood cells flowing inside SC. We also segmented SC from half of the vis-OCT volume and overlaid the segmented SC (pseudo-colored in yellow) onto the vis-OCTA volume (semitransparent gray). Both the segmented results and vis-OCTA results of the blood-refluxed SC showed near-perfect overlap, confirming that our semiautomatic segmentation faithfully detected SC from vis-OCT images. Indeed, after segmenting the projected vis-OCTA volume to remove most of the vessels surrounding SC, the overlap between the projected vis-OCTA SC and the projected segmented SC, as quantified by the Dice coefficient, was 0.87, implying good agreement.

Figure 6 shows the results of imaging the full SC under elevated EVP and the associated limbal microvascular network using our compound circumlimbal scan as illustrated in Figure 2e. We acquired eight raster scans using vis-OCTA, rotating the attachment 45° between each raster scan. The final montaged images projected onto a sphere, forming the circumlimbal view, are shown in Figure 6a. Figure 6b is a projection view of the four quadrants of the entire SC and limbal microvascular network, mimicking the commonly used flat-mount microscopic images.[39] The superficial limbus vasculature is color-coded in the left quadrant, by matching anatomical features with previously published histologic studies.[40]

Discussion

We demonstrate, for the first time, in vivo imaging of the entire SC and its surrounding limbal microvascular network in mice. We developed an oblique-incident vis-OCT system to accommodate the curvature of the eyeball for the best SC imaging quality. We empirically identified that the best imaging angle between the vis-OCT incident light beam and the optical axis of the eye is approximately 60° from the optical axis. To avoid rotating the mouse and the associated unwanted perturbations in both IOP and EVP, we added a two-mirror assembly that was rotated about the optical axis of the eye. We used a 3D-printed phantom eyeball to calibrate the geometries of this rotational scanning setup for full-field SC structure reconstruction. We found that each raster scan of 1.8 × 1.8 mm^2 can cover approximately 20% of the total SC perimeter, and eight rotations of the raster scan will ensure adjacent images to have sufficient overlap for circumlimbal 3D reconstruction and montage.

In our study, we used two methods, manometry to change IOP and blood reflux, to validate the capability of our vis-OCT system on noninvasive imaging of SC and its size alterations. Several studies on both mouse and human support the observation that there is a large variation in SC cross-sectional area in a single subject, which is further dependent upon IOP, physical exercises, glaucomatous status, blood reflux, and congenital abnormalities.[41–45] We visualized such

Investigative Ophthalmology & Visual Science

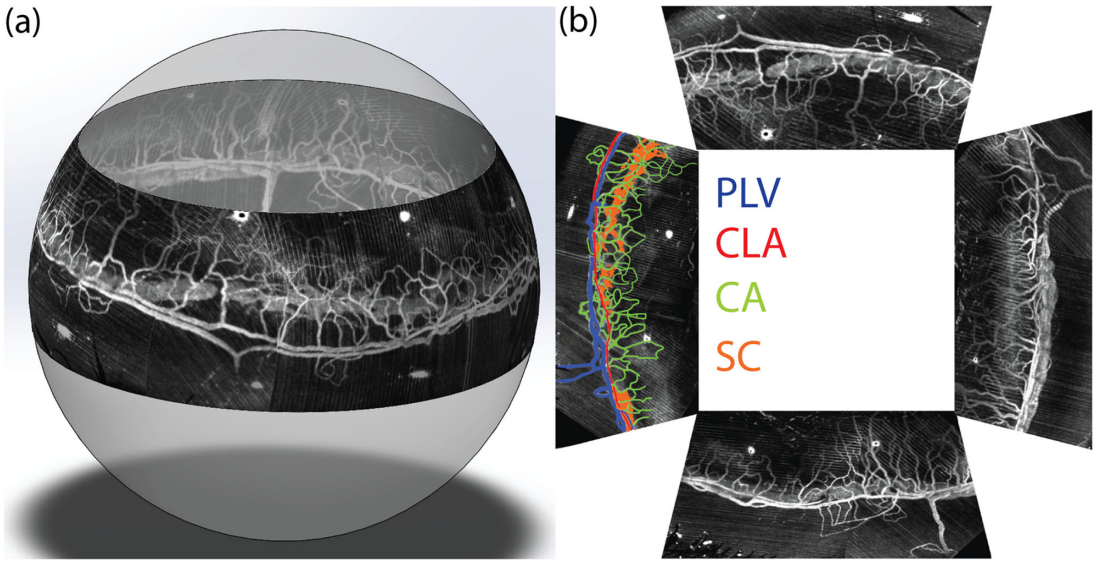

Figure 6. (**a**) 3D visualization of montaged vis-OCTA circumlimbal image of SC under elevated EVP and the surrounding limbal microvascular network (see Supplementary Video S2). (**b**) Projection view of the imaged entire SC and limbal microvascular network in the flat-mount style four quadrants. The left quadrant is pseudo-colored to highlight different anatomical features of the limbal microvessels. PLV, perilimbal vein; CLA, circular limbal artery; CA, corneal arcades; SC, Schlemm's canal.

rapid changes in SC cross-sectional area within a 1-mm section of the mouse SC in the 3D surface rendering (Fig. 3b).

Using manometry, we confirmed that cross-sectional area can vary significantly even within a short 1.5-mm section of SC (Fig. 4m). Indeed, periodic peaks are visible roughly every 400 μm, and the locations of these peaks remain consistent throughout the IOP-level changes. As it has been reported in humans that aqueous outflow is increased near the collector channels, and SC is known to have a larger cross-sectional area near the collector channels,[46] these peaks may coincide with the locations of collector channels in mouse. Thus, cautions should be taken when considering tracking SC alterations according to only a few B-scans. Instead, the volume of a given section of SC should be more reliable for quantitative analysis of SC changes. Our results show that SC volume significantly decreased with the IOP elevation (Fig. 4n) and demonstrate that even in wild-type mice, a 10-mm Hg increase in IOP leads to nearly total collapse of SC according to vis-OCT image (Figs. 4g and 4l). Figure 4n shows an average reduction of 72% at Δ+10 mm Hg and 26% reduction at Δ+5 mm Hg. As reported by Li et al.,[25] the SC size reduces roughly 80% at 20 mm Hg and 37% at 15 mm Hg. Li et al.[25] did not set the IOP levels relative to baseline IOP but rather at absolute values. Regardless, the values obtained are comparable to the degree of collapse that we observed. We recognize that there exists room for error in measuring SC cross-sectional area due to segmentation inaccuracy, limitations of vis-OCT resolution, and influence from signal-to-noise ratio and speckles. The inverse relationship between IOP and SC cross-sectional size in wild-type mice matches well with previously published human studies.[47,48] Several clinical studies have shown that SC is smaller in glaucomatous eyes as compared with normal eyes, and it is thought that decreased SC lumen size contributes to the elevated pressure characteristic of primary open-angle glaucoma.[13,44,48,49]

Some researchers consider visualization of the blood in SC after sclera compression as a positive prognosis factor of successful antiglaucoma surgery.[14,15] Blood refluxed into SC may reflect the communication between the episcleral veins and SC. The mouse blood reflux test was performed by increasing the pressure of the episcleral vein, causing the blood to flow in the reverse direction of its usual flow and enter SC. Through vis-OCT imaging, blood reflux directly increased SC size after episcleral vein blockage. Additionally, the refluxed blood in SC also shows positive signal in vis-OCTA, thus allowing us to directly visualize SC without segmentation or introducing any exogenous contrast agent.[50] Although several publications have used OCTA to image the SC in mouse, only B-scan images were shown and the angiography information was used as a tool in segmenting the SC rather than enabling direct visualization of SC.[24–26] Although not in its natural physiologic state, the entire structure of SC can be noninvasively and fully reconstructed. Therefore, the enlargement of SC and its uniformity under external perturbation imaged by OCT may be a potential measure to predict the success of certain antiglaucoma surgeries such as laser trabeculoplasty and canaloplasty.[14,15]

The perilimbal vein (PLV), pseudo-colored in blue in Figure 6b, has been described as a plexus forming a continuous ring around the limbus.[40] These features of the PLV are evident in the circumlimbal scan. The circular limbal artery (CLA), pseudo-colored in red in Figure 6a, is described as a single narrow artery, which can often be found with the PLV.[40] The corneal arcades (CAs), pseudo-colored in green, are looped vessels that anastomose with both CLA and PLV.[40] Therefore, the CAs can be considered capillary equivalents in the limbal vasculature. Finally, SC (pseudo-colored in orange) often but not always runs directly parallel to the superficial limbal vasculature.

In summary, our findings demonstrate that we can image the entirety of SC and its surrounding limbal microvascular network in mice using vis-OCT and vis-OCTA. In agreement with other investigations,[51,52] we found that at normal IOP, SC is a continuous structure that extends around the limbus. In the future, we will investigate the size variation in normal

SC and validate vis-OCT measurement by histologic analysis as well as electron microscopy. We will further investigate the hemodynamics of the limbal microvascular network under changing IOP levels. We believe that vis-OCT has the potential to shed new light on investigating the conventional outflow pathway in both healthy and glaucomatous eyes.

Acknowledgments

The authors thank Pieter Norden and Benjamin Thomson for helpful discussions.

Supported in part by National Institutes of Health grants R01EY026078, DP3DK108248, R01EY029121, R01EY028304, R44EY026466, P30 EY016665, and T32EY25202; a Cornew Innovation Award from the Chemistry of Life Processes Institute at Northwestern University; the National Science Foundation Graduate Research Fellowship 1000260620 (LB); and RPB Stein Innovation Award, an award from RPB to the Department of Ophthalmology, University of Wisconsin-Madison (NS).

Disclosure: **X. Zhang**, None; **L. Beckmann**, None; **D.A. Miller**, None; **G. Shao**, None; **Z. Cai**, None; **C. Sun**, Opticent, Inc. (F); **N. Sheibani**, None; **X. Liu**, None; **J. Schuman**, Opticent, Inc. (F); **M. Johnson**, None; **T. Kume**, None; **H.F. Zhang**, Opticent, Inc. (F)

References

1. Tham YC, Li X, Wong TY, Quigley HA, Aung T, Cheng CY. Global prevalence of glaucoma and projections of glaucoma burden through 2040: a systematic review and meta-analysis. *Ophthalmology*. 2014;121:2081–2090.
2. Sommer A. Collaborative normal-tension glaucoma study. *Am J Ophthalmol*. 1999;128:776–777.
3. Sommer A, Tielsch JM, Katz J, et al. Relationship between intraocular pressure and primary open angle glaucoma among white and black americans: the Baltimore Eye Survey. *JAMA Ophthalmol*. 1991;109:1090–1095.
4. The advanced glaucoma intervention study (AGIS): 7. the relationship between control of intraocular pressure and visual field deterioration. *Am J Ophthalmol*. 2000;130:429–440.
5. Roy Chowdhury U, Hann CR, Stamer WD, Fautsch MP. Aqueous humor outflow: dynamics and disease. *Invest Ophth Vis Sci*. 2015;56:2993–3003.
6. Goel M, Picciani RG, Lee RK, Bhattacharya SK. Aqueous humor dynamics: a review. *Open Ophthalmol J*. 2010;4:52–59.
7. Johnstone MA, Grant WG. Pressure-dependent changes in structures of the aqueous outflow system of human and monkey eyes. *Am J Ophthalmol*. 1973;75:365–383.
8. Carreon T, van der Merwe E, Fellman RL, Johnstone M, Bhattacharya SK. Aqueous outflow—a continuum from trabecular meshwork to episcleral veins. *Prog Retinal Eye Res*. 2017;57:108–133.
9. Johnson M. 'What controls aqueous humour outflow resistance?'. *Exp Eye Res*. 2006;82:545–557.
10. Lai J, Su Y, Swain DL, Huang D, Getchevski D, Gong H. The role of Schlemm's canal endothelium cellular connectivity in giant vacuole formation: a 3D electron microscopy study. *Invest Ophthalmol Vis Sci*. 2019;60:1630–1643.
11. Allingham RR, de Kater AW, Ethier RC. Schlemm's canal and primary open angle glaucoma: correlation between Schlemm's canal dimensions and outflow facility. *Exp Eye Res*. 1996;62:101–110.
12. Battista SA, Lu Z, Hofmann S, Freddo T, Overby DR, Gong H. Reduction of the available area for aqueous humor outflow and increase in meshwork herniations into collector channels following acute IOP elevation in bovine eyes. *Invest Ophthalmol Vis Sci*. 2008;49:5346–5352.
13. Johnson MC, Kamm RD. The role of Schlemm's canal in aqueous outflow from the human eye. *Invest Ophthalmol Vis Sci*. 1983;24:320–325.
14. Gong J-L, Al-Wesabi SA, Zhao Y, Zhang H. Positive correlation between blood reflux in Schlemm's canal and the decrease of intraocular pressure after selective laser trabeculoplasty in primary open-angle glaucoma. *Exp Ther Med*. 2018;15:5065–5069.
15. Grieshaber MC, Pienaar A, Olivier J, Stegmann R. Clinical evaluation of the aqueous outflow system in primary open-angle glaucoma for canaloplasty. *Invest Ophthalmol Vis Sci*. 2010;51:1498–1504.
16. Adhi M, Duker JS. Optical coherence tomography—current and future applications. *Curr Opin Ophthalmol*. 2013;24:213–221.
17. Ang M, Baskaran M, Werkmeister RM, et al. Anterior segment optical coherence tomography. *Prog Retinal Eye Res*. 2018;66:132–156.
18. Sakata LM, Deleon-Ortega J, Sakata V, Girkin CA. Optical coherence tomography of the retina and optic nerve—a review. *Clin Exp Ophthalmol*. 2009;37:90–99.
19. Chen Z, Sun J, Li M, et al. Effect of age on the morphologies of the human Schlemm's canal and trabecular meshwork measured with sweptsource optical coherence tomography. *Eye (Lond)*. 2018;32:1621–1628.
20. Fernandez-Vigo JI, Kudsieh B, De-Pablo-Gomez-de-Liano L, et al. Schlemm's canal measured by optical coherence tomography and correlation study in a healthy Caucasian child population. *Acta Ophthalmol*. 2019;97:e493–e498.
21. Imamoglu S, Sevim MS, Alpogan O, et al. In vivo biometric evaluation of Schlemm's canal with spectral-domain optical coherence tomography in pseuduexfoliation glaucoma. *Acta Ophthalmol*. 2016;94:e688–e692.
22. Usui T, Tomidokoro A, Mishima K, et al. Identification of Schlemm's canal and its surrounding tissues by anterior segment Fourier domain optical coherence tomography. *Invest Ophthalmol Vis Sci*. 2011;52:6934–6939.
23. Li G, Farsiu S, Chiu SJ, et al. Pilocarpine-induced dilation of Schlemm's canal and prevention of lumen collapse at elevated intraocular pressures in living mice visualized by OCT. *Invest Ophthalmol Vis Sci*. 2014;55:3737–3746.
24. Li G, Farsiu S, Chiu SJ, et al. Pilocarpine-induced dilation of Schlemm's canal and prevention of lumen collapse at elevated intraocular pressures in living mice visualized by OCT. *Invest Ophthalmol Vis Sci*. 2014;55:3737–3746.
25. Li G, Lee C, Agrahari V, et al. In vivo measurement of trabecular meshwork stiffness in a corticosteroid-induced ocular hypertensive mouse model. *Proc Natl Acad Sci*. 2019;116:1714.
26. Li G, Mukherjee D, Navarro I, et al. Visualization of conventional outflow tissue responses to netarsudil in living mouse eyes. *Eur J Pharmacol*. 2016;787:20–31.
27. Aihara M, Lindsey JD, Weinreb RN. Episcleral venous pressure of mouse eye and effect of body position. *Curr Eye Res*. 2003;27:355–362.
28. Shu X, Beckmann L, Zhang H. Visible-light optical coherence tomography: a review. *J Biomed Opt*. 2017;22:1–14.
29. Hariri S, Johnstone M, Jiang Y, et al. Platform to investigate aqueous outflow system structure and pressure-dependent motion using high-resolution spectral domain optical coherence tomography. *J Biomed Opt*. 2014;19:106013–106013.

Investigative Ophthalmology & Visual Science

30. Huang AS, Francis BA, Weinreb RN. Structural and functional imaging of aqueous humour outflow: a review. *Clin Exp Ophthalmol*. 2018;46:158–168.
31. Yi J, Chen S, Backman V, Zhang HF. In vivo functional microangiography by visible-light optical coherence tomography. *Biomed Opt Express*. 2014;5:3603–3612.
32. Yi J, Wei Q, Liu W, Backman V, Zhang HF. Visible-light optical coherence tomography for retinal oximetry. *Opt Lett*. 2013;38:1796–1798.
33. Danias J, Kontiola AI, Filippopoulos T, Mittag T. Method for the noninvasive measurement of intraocular pressure in mice. *Invest Ophthalmol Vis Sci*. 2003;44:1138–1141.
34. Soille P. *Morphological Image Analysis: Principles and Applications*. New York: Springer; 1999.
35. Koo TK, Li MY. A guideline of selecting and reporting intraclass correlation coefficients for reliability research. *J Chiropr Med*. 2016;15:155–163.
36. Chen S, Liu Q, Shu X, Soetikno B, Tong S, Zhang HF. Imaging hemodynamic response after ischemic stroke in mouse cortex using visible-light optical coherence tomography. *Biomed Opt Express*. 2016;7:3377–3389.
37. Dice LR. Measures of the amount of ecologic association between species. *Ecology*. 1945;26:297–302.
38. Fedorov A, Beichel R, Kalpathy-Cramer J, et al. 3D Slicer as an image computing platform for the Quantitative Imaging Network. *Magn Reson Imaging*. 2012;30:1323–1341.
39. Thuret G, He Z. Flat-mount preparation of cornea [published online September 7, 2017]. *Acta Ophthalmol*.
40. van der Merwe EL, Kidson SH. The three-dimensional organisation of the post-trabecular aqueous outflow pathway and limbal vasculature in the mouse. *Exp Eye Res*. 2014;125:226–235.
41. Kizhatil K, Ryan M, Marchant JK, Henrich S, John SWM. Schlemm's canal is a unique vessel with a combination of blood vascular and lymphatic phenotypes that forms by a novel developmental process. *PLoS Biol*. 2014;12:e1001912.
42. Truong TN, Li H, Hong Y-K, Chen L. Novel characterization and live imaging of Schlemm's canal expressing Prox-1. *PLoS One*. 2014;9:e98245.
43. Moses RA, Hoover GS, Oostwouder PH. Blood reflux in Schlemm's canal. I. Normal findings. *Arch Ophthalmol*. 1979;97:1307–1310.
44. Tandon A, Watson C, Ayyala R. Ultrasound biomicroscopy measurement of Schlemm's canal in pediatric patients with and without glaucoma. *J AAPOS*. 2017;21:234–237.
45. Kagemann L, Nevins JE, Jan N-J, et al. Characterisation of Schlemm's canal cross-sectional area. *Br J Ophthalmol*. 2014;98:ii10.
46. Kagemann L, Wollstein G, Ishikawa H, et al. Identification and assessment of Schlemm's canal by spectral-domain optical coherence tomography. *Invest Ophthalmol Vis Sci*. 2010;51:4054–4059.
47. Kagemann L, Wang B, Wollstein G, et al. IOP elevation reduces Schlemm's canal cross-sectional area. *Invest Ophthalmol Vis Sci*. 2014;55:1805–1809.
48. Yan X, Li M, Chen Z, Zhu Y, Song Y, Zhang H. Schlemm's canal and trabecular meshwork in eyes with primary open angle glaucoma: a comparative study using high-frequency ultrasound biomicroscopy. *PLoS One*. 2016;11:e0145824.
49. Allingham RR, de Kater AW, Ethier CR. Schlemm's canal and primary open angle glaucoma: correlation between Schlemm's canal dimensions and outflow facility. *Exp Eye Res*. 1996;62:101–109.
50. Huang AS, Mohindroo C, Weinreb RN. Aqueous humor outflow structure and function imaging at the bench and bedside: a review. *J Clin Exp Ophthalmol*. 2016;7:pii 578.
51. van der Merwe EL, Kidson SH. The three-dimensional organisation of the post-trabecular aqueous outflow pathway and limbal vasculature in the mouse. *Exp Eye Res*. 2014;125:226–235.
52. Kizhatil K, Ryan M, Marchant JK, Henrich S, John SW. Schlemm's canal is a unique vessel with a combination of blood vascular and lymphatic phenotypes that forms by a novel developmental process. *PLoS Biol*. 2014;12:e1001912.

Supplementary Material

Supplementary Video S1. Video showing the 3D visualization of the 1mm length of segmented SC from Figure 3b.

Supplementary Video S2. Video showing the 3D visualization of the montaged vis-OCTA circumlimbal image of SC under elevated EVP and the surrounding limbal microvascular network from Figure 6a.

Investigative Ophthalmology & Visual Science